energies

MDPI

Article

Fuzzy Super-Twisting Sliding Mode Controller for Switched Reluctance Wind Power Generator in Low-Voltage DC Microgrid Applications

Zeineb Touati [1], Imed Mahmoud [2], Rui Esteves Araújo [3,*] and Adel Khedher [1]

[1] LATIS—Laboratory of Advanced Technology and Intelligent Systems, National Engineering School of Sousse, University of Sousse, Sousse 4023, Tunisia; zeineb.touati@eniso.u-sousse.tn (Z.T.); adel.khedher@eniso.u-sousse.tn (A.K.)
[2] LATIS—Laboratory of Advanced Technology and Intelligent Systems, Higher Institute of Applied Sciences and Technology of Mahdia, University of Monastir, Mahdia 5121, Tunisia; mahmoud.imed@issatm.rnu.tn
[3] Institute for Systems and Computer Engineering, Technology and Science (INESC TEC) and Faculty of Engineering, University of Porto, 4200-465 Porto, Portugal
* Correspondence: raraujo@fe.up.pt

Abstract: There is limited research focused on achieving optimal torque control performance of Switched Reluctance Generators (SRGs). The majority of existing studies tend to favor voltage or power control strategies. However, a significant drawback of SRGs is their susceptibility to high torque ripple. In power generation systems, torque ripple implicates fluctuations in the generated power of the generator. Moreover, high torque ripple can lead to mechanical vibrations and noise in the powertrain, impacting the overall system performance. In this paper, a Torque Sharing Function (TSF) with Indirect Instantaneous Torque Control (IITC) for SRG applied to Wind Energy Conversion Systems (WECS) is proposed to minimize torque ripple. The proposed method adjusts the shared reference torque function between the phases based on instantaneous torque, rather than the existing TSF methods formulated with a mathematical expression. Additionally, this paper introduces an innovative speed control scheme for SRG drive using a Fuzzy Super-Twisting Sliding Mode Command (FSTSMC) method. Notably robust against parameter uncertainties and payload disturbances, the proposed scheme ensures finite-time convergence even in the presence of external disturbances, while effectively reducing chattering. To assess the effectiveness of the proposed methods, comprehensive comparisons are made with traditional control techniques, including Proportional–Integral (PI), Integral Sliding Mode Control (ISMC), and Super-Twisting Sliding Mode Control (STSMC). The simulation results, obtained using MATLAB®/SIMULINK® under various speeds and mechanical torque conditions, demonstrate the superior performance and robustness of the proposed approaches. This study presents a thorough experimental analysis of a 250 W four-phase 8/6 SRG. The generator was connected to a DC resistive load, and the analysis focuses on assessing its performance and operational characteristics across different rotational speeds. The primary objective is to validate and confirm the efficacy of the SRG under varying conditions.

Keywords: wind energy conversion; switched reluctance generator; torque control; sliding mode control; fuzzy control

Citation: Touati, Z.; Mahmoud, I.; Araújo, R.E.; Khedher, A. Fuzzy Super-Twisting Sliding Mode Controller for Switched Reluctance Wind Power Generator in Low-Voltage DC Microgrid Applications. *Energies* **2024**, *17*, 1416. https://doi.org/10.3390/en17061416

Academic Editor: Frede Blaabjerg

Received: 20 February 2024
Revised: 7 March 2024
Accepted: 12 March 2024
Published: 15 March 2024

1. Introduction

Electric energy plays an important role in the economic development of all countries. Over the last decade, a rapid increase in electricity consumption and demand has been recorded [1]. In addition, low-voltage DC microgrids can be very useful for people living in rural areas in the context of weak grid connectivity. Thus, renewable energy, such as that obtained using Wind Energy Conversion Systems (WECS) and DC microgrids, seems to be an adequate solution to simultaneously meet the demand for energy while decreasing

environmental pollution and toxic materials and to promote a cost-effective solution for energy access and off-grid systems [2]. Furthermore, the research community has invested great effort into making sources efficient safe and effective [3]. The presented work is a step in the same direction. Nowadays, microgrids, based on renewable sources and energy storage units, can be used to reduce fossil fuel and carbon dioxide consumption [4,5]. Power-generating machines are integral components in various systems, including wind and hydroelectric systems and electric and hybrid vehicles [6,7]. The Switched Reluctance Generator (SRG) is becoming a relevant alternative for WECS applications due to its simplicity of construction, robustness, wide speed range, and absence of magnets in its design [8,9]. The use of SRGs in the above-mentioned applications presents a number of challenges, which are currently the subject of research by the technical and scientific community. These challenges include the highly non-linear nature of the machine, high acoustic noise, low efficiency at low speeds, and, above all, high torque ripple [10,11].

A review of the literature shows that most research on SRGs has focused on the study of power and voltage controllers [12,13]. In [14], the authors developed a method to control the DC microgrid with an SRG. Direct power control has been used to achieve the maximum power transfer of the wind system. In [15], a bidirectional DC-DC converter was adopted as an interface stage between the SRG and the grid to achieve optimal excitation voltage at the SRG side, while a voltage source converter regulates the DC-bus voltage. The authors demonstrate that the proposed control improved the quality of the power supply, which is reflected in the grid current. Moreover, a proportional resonant control strategy was proposed in [16] to improve the response of the SRG output voltage compared to the conventional Proportional–Integral (PI) system. In [17], a first-order sliding mode controller has been proposed and evaluated for control of SRG voltage. Furthermore, the authors in [18] proposed a Sliding Mode Controller (SMC) with parameter optimization based on a genetic algorithm to build and adjust the output voltage of SRGs. Nevertheless, appropriate techniques for reducing torque ripple for machines operating as generators are rarely discussed in the literature, but numerous recent publications have addressed torque control in reluctance motors [19–21]. Various control strategies, including Indirect Instantaneous Torque Control (IITC), Torque Sharing Function (TSF), and Direct Torque Control (DTC), have been explored either independently or in a combined manner. The integration of these strategies aims to capitalize on their unique characteristics across specific speed ranges, aiming for outcomes such as reduced torque ripple, enhanced efficiency, and an elevated current torque ratio [22]. In [23], the authors developed an DITC and a maximum power point tracking technique for a 12/8 switched reluctance generator-based wind turbine in order to optimize the overall performance. Several research studies have employed methodologies to improve the efficiency of SRGs through the optimization of algorithms and parameters. In [24], a specific algorithm for maximum power point tracking was devised. This algorithm is designed to identify the optimal parameters of SRG 12/8, taking into account the mechanical energy. In [25], the proposed approach involves the application of direct average torque control for SRG in WECS. A non-unity TSF was suggested in [26] to effectively reduce torque ripple across a broad operational speed range for SRG. However, it is essential to note that the objective was not only to enhance power generation but also to address issues such as curbing current fluctuations and minimizing torque ripple. This was achieved through the implementation of diverse control strategies for SRGs. It is crucial to emphasize that the selection of these performance indices should be driven by specific system requirements and approached with a comprehensive optimization perspective.

Conventional speed control methods for switched reluctance machines based on linear controllers perform adequately in many applications but face limitations, such as variations in machine parameters. To overcome these challenges and enhance precision, numerous innovative nonlinear control strategies have been proposed over the years [27]. Among these methods, Fuzzy Logic Control (FLC) excels at handling uncertainties and variations in machine parameters. By incorporating linguistic variables and employing rule-based reasoning, FLC dynamically adapts to the changing conditions of the system, offering a

more robust and adaptable control mechanism. Some papers in this field are presented to improve the control of the wind energy conversion system. In [28], a fuzzy (Takagi–Sugeno) controller, optimized by genetic algorithms, was implemented to enhance the stability of a wind turbine's power output. This ensured more efficient protection against harmful wind speeds, thereby extending the turbine's durability and reducing energy production costs. The authors in [29] focus on the sustainable revitalization of the Canal de Castilla, employing a community-focused approach. They assessed the implementation of hydroelectric turbines using fuzzy logic, which solidified the feasibility of integrating axial turbines into the canal's ecosystem.

Another noteworthy approach is Sliding Mode Control (SMC), a nonlinear robust control method proven effective in systems with parameter uncertainties. Scholars have introduced various SMC variants with specific sliding surface forms for industrial systems. In [30], the authors introduced a fuzzy sliding mode controller, which merges the smart features of fuzzy logic with the SMC technique. Additionally, in [31], the authors introduced an innovative speed control scheme for SR motors based on a fast terminal sliding mode control method. The gain value of a sign function is significantly diminished by combining the suggested fast terminal SMC with a fuzzy logic compensator.

However, SMC has drawbacks, including an undesirable chattering effect, which can be detrimental to the system. To overcome this, second-order sliding mode algorithms have been explored, inheriting SMC properties while mitigating chattering and high-frequency vibrations [32]. Nonlinear Super-Twisting Sliding Mode Control (STSMC) have recently gained attention for various systems. These methods ensure the robustness and finite-time convergence of nonlinear systems when the attractiveness condition is met. STSMC mitigates chattering and vibrations, reducing mechanical stresses in the system. Previous works, such as those in [32,33], analyze second-order sliding mode control with the super-twisting algorithm. The objective is to explore the theoretical background of second-order sliding mode control, present new findings, and to show that the STSMC approach is an effective solution to the above-cited drawbacks and may constitute a good candidate for solving a wide range of important practical problems

The primary objectives of our work are to propose indirect instantaneous torque control for an 8/6 SRG based on the TSF, aiming to address torque ripple reduction and enhance the overall efficiency. A novel approach, the Fuzzy Super-Twisting Sliding Mode Command (FSTSMC) method, is introduced, combining fuzzy logic and the super-twisting algorithm for precise speed control. This method is specifically tailored to generate a reference torque, optimizing the SRG's performance by minimizing the convergence time for tracking error and ensuring high robustness against external disturbances and parameter uncertainties. Additionally, the integration of FSTSMC with fuzzy logic mitigates chattering effects, thereby significantly reducing the control gain of a sign function. The experimental validation, conducted on an SRG within a low-voltage DC microgrid, provides valuable insights into the discussed control techniques. The utilization of a variable resistive load in the experiments emulates real-world scenarios connected to the DC bus, enhancing the practical relevance of our study.

This paper is structured as follows: Section 2 is entirely focused on the modeling of a turbine and generator, followed by the design of the proposed torque control based on torque sharing function in Section 3. In Section 4, the PI speed controller, the ISMC, the STSMC, and the FSTSMC are developed. In Section 5, the simulation results are given and discussed. In Section 6, the experimental results are presented. Finally, in Section 7, conclusions are extracted.

2. Mathematical Model and Operation of SRG

2.1. Theoretical Background of the SRG

The generator mode function requires an external voltage source for initial phase magnetization due to the totally passive nature of the SRG rotor (no winding, no magnet). A battery in series with a diode is placed on the DC bus to energize the machine at start-up.

The diode prevents current return to the battery during the generation mode. When the capacitor voltage becomes sufficiently high, the battery is automatically disconnected, and the excitation current is supplied by the capacitor. No energy is now drawn from the battery. This is called self-excitation of the generator. The excitation process of each SRG phase consists of two regions: magnetization and demagnetization. During magnetization, switches S_1 and S_2 are concurrently activated, injecting a phase current. To regulate the current, S_2 is deactivated when the phase current surpasses the maximum allowable current. This mode, known as the freewheeling mode, enables damping of the phase current through the phase resistance. As the magnetization phase concludes, demagnetization initiates by deactivating both S_1 and S_2, causing a reversal in the phase voltage ($-V_{dc}$). During this phase, the phase current is redirected to the source by activating D_1 and D_2. Additionally, the phase current reaches zero prior to reaching the aligned position. The one-phase switching actions are detailed in Table 1, providing a comprehensive overview of the excitation process.

Table 1. Single-phase operation of SRG.

Operating Mode	Switches Active	Phase Voltage (V_k)	State
Magnetization	S_1, S_2	V_{dc}	Excitation
	S_1, D_1 or S_2, D_2	0	Freewheeling
Demagnetization	D_1, D_2	$-V_{dc}$	Generation

The profiles of the inductance, phase current, and voltage as functions of the rotor position in the two regions are illustrated in Figure 1. The regulation of current involves the application of a hysteresis controller with a designated hysteresis band, denoted as Δi.

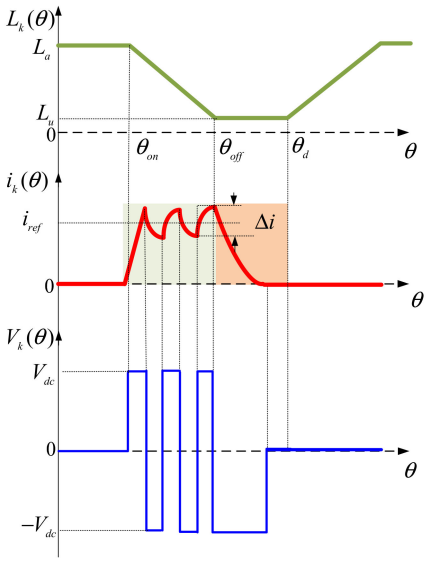

Figure 1. Typical evolution of inductance (green), phase current (red), and phase voltage (blue) as functions of rotor position.

The selection of the activation and deactivation angles θ_{on} and θ_{off} plays a key role in SRG performance. These angles must be set between the aligned and the unaligned θ_d position. The precise determination of these angles is important for achieving optimal current regulation and ensuring seamless operation of the generator throughout its operational range.

The fundamental differential equations of SRG can be expressed as follows [34,35]:

$$J\dot{\omega}_r = T_M - T_e - f\omega_r \quad (1)$$

$$\dot{i}_k = \left(V_k - r_k i_k + \frac{\partial \lambda_k(\theta, \mathrm{i}_k)}{\partial \theta}\omega_r\right)\left(\frac{\partial \lambda_k(\theta, \mathrm{i}_k)}{\partial \mathrm{i}_k}\right)^{-1} \quad k = 1,2,3,4 \tag{2}$$

$$\dot{\theta} = \omega_r \tag{3}$$

where

ω_r is the angular speed of a prime mover;
T_e is the electromagnetic torque of the SRG;
T_M is the mechanical torque;
f is the coefficient of friction;
J is the moment of inertia;
θ is the rotor position;
i_k is the current of the kth phase of the SRG;
V_k is the voltage of the kth phase of the SRG;
$\lambda_k(\theta,i)$ is the flux linkage of the kth phase of the SRG;
r_k is the resistance of the kth phase of the SRG.

From the mechanical equation expressed in Equation (1), it is evident that the sign of the mechanical torque is positive, attributed to the operational nature of the switched reluctance machine acting as a generator. The inductance and torque curve for different values of the current and rotor position are shown in Figure 2. Therefore, the flux linkage and torque can be calculated using co-energy according to the following equation:

$$T_e(\theta, \mathrm{i}_k) = \sum_{k=1}^{4} T_k(\theta, \mathrm{i}_k) \tag{4}$$

$$T_k(\theta, \mathrm{i}_k) = \left[\frac{\partial W_k(\theta, \mathrm{i}_k)}{\partial \theta}\right]_{i_{k=const}} \quad k = 1,2,3,4 \tag{5}$$

$$W_k(\theta, \mathrm{i}_k) = \int_0^{i_k} \lambda_k(\theta, \mathrm{i}_k)\, di_k \tag{6}$$

where

$$\lambda_k(\theta, \mathrm{i}_k) = L_k(\theta, \mathrm{i}_k)\, \mathrm{i}_k \tag{7}$$

where T_k, W_k, and L_k are the torque, co-energy, and inductance of the kth phase, respectively. The torque of the kth phase can be calculated based on the above equations.

$$T_k(\theta, \mathrm{i}_k) = \frac{1}{2} i_k^2 \frac{dL_k(\theta)}{d\theta} \tag{8}$$

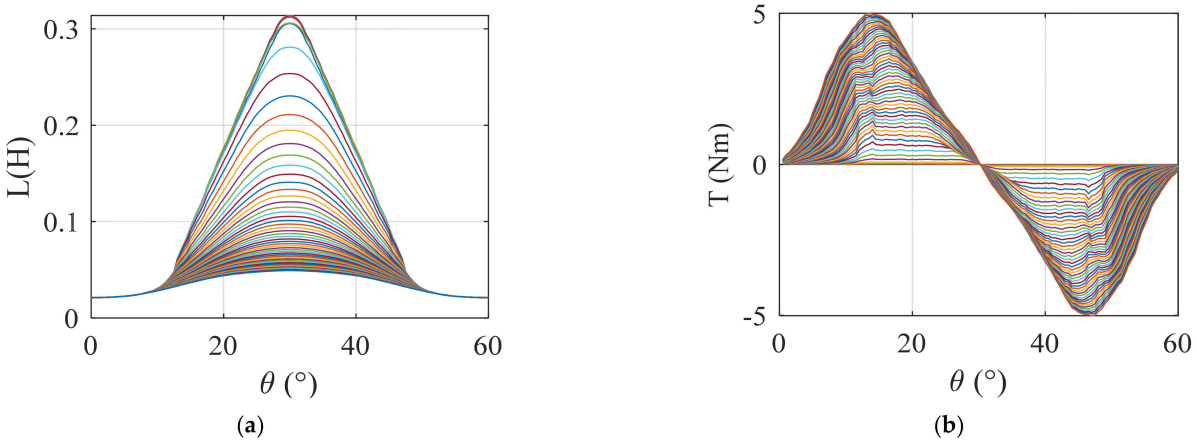

Figure 2. Characteristics of 8/6 SRG: (**a**) inductance; (**b**) torque.

2.2. Conversion of Wind Energy

For a wind turbine with a blade radius of R meters and a pitch angle of β, the captured mechanical power (P_t) from the wind at any wind speed (V_t in m/s) is expressed as follows [36,37]:

$$P_t = \frac{1}{2} C_p(\beta, \lambda) \rho \pi R^2 v_t^3 \tag{9}$$

The wind power coefficient is limited by the design of the wind turbine. The power coefficient is defined by [36]:

$$C_p(\beta, \lambda) = C_1 \left(\frac{C_2}{\lambda i} - C_3 \beta - C_4 \right) e^{-\frac{C_5}{\lambda i}} + C_6 \lambda \tag{10}$$

$$\frac{1}{\lambda i} = \left(\frac{1}{\lambda + 0.08\beta} - \frac{0.035}{\beta^3 + 1} \right) \tag{11}$$

The coefficients C_1 to C_6 are: $C_1 = 0.5176, C_2 = 116, C_3 = 0.4, C_4 = 5, C_5 = 21$, $C_6 = 0.0068$. The ratio λ is a function of v_t, wind speed (rad/s), and rotor radius and is expressed as [37],

$$\lambda = \frac{\omega_r R}{v_t} \tag{12}$$

The characteristics of the selected wind turbine are shown in Figure 3. The maximum electrical power is generated by the wind at any given wind speed, when Cp reaches its maximum. The power coefficient reaches its maximum value (0.42) only at a tip speed ratio (λ_{opt}) of 8, as shown in Figure 3a. Hence, the first priority is to adjust the wind speed to the rotor speed in order to obtain a better conversion efficiency, which is represented by a maximum Cp. Thus, the optimal power curve can be calculated as follows [38]:

$$P_{t-opt} = K_{opt} . \omega_r^3 \tag{13}$$

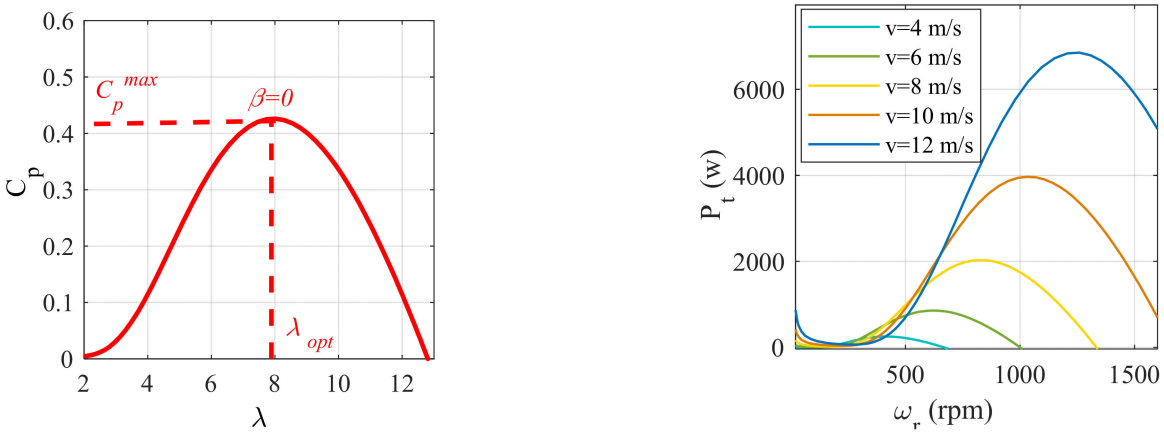

Figure 3. Wind turbine characteristics. (**a**) Cp as a function of λ and β; (**b**) output power as a function of speed for different wind speeds.

3. IITC Based on Torque Sharing Function

Torque control methods can be divided into direct and indirect categories according to the type of feedback state variable used. Direct torque control requires torque regulation based on feedback from the direct torque estimate, while the indirect method relies on feedback from the phase current [39]. The indirect instantaneous torque control method is classified as the current profiling and TSF methods [40]. The current profiling technique essentially determines the reference currents to control the torque. These reference phase currents are determined without using the current vs. position and torque LUT. Hence, TSF

is a favorable indirect torque control method, as it is simple and has low computational burden. The total torque is shared among the commutating phases. Figure 4 illustrates the block diagram of the IITC torque control based on the TSF method for a four-phase SRG.

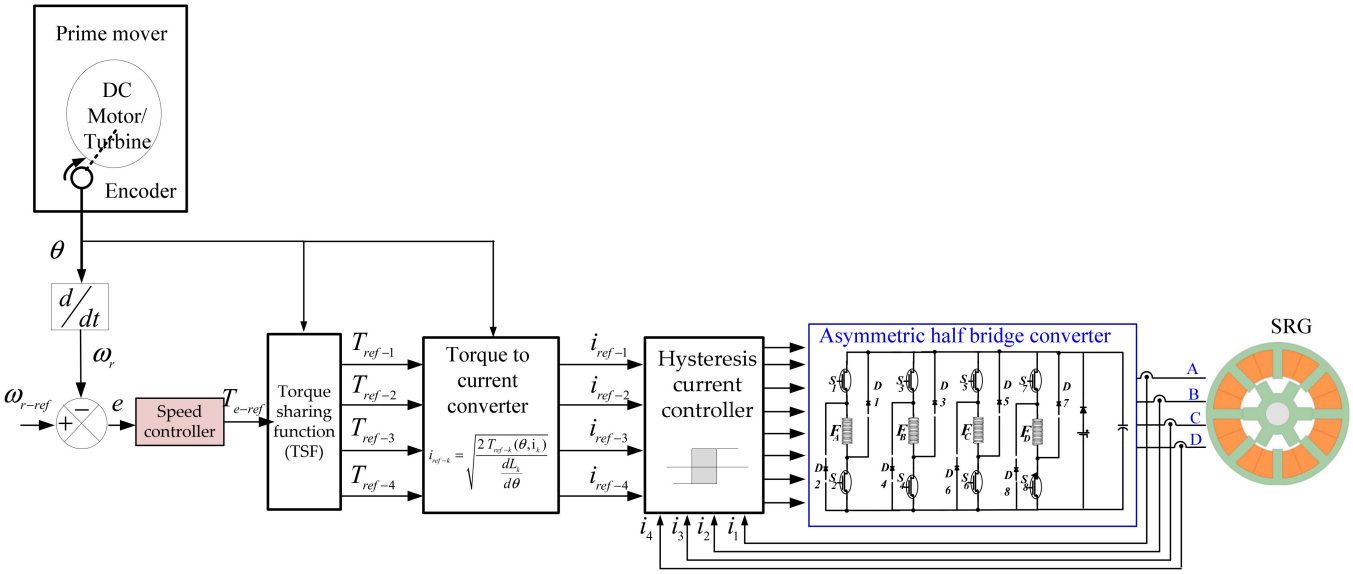

Figure 4. The block diagram of the TSF torque control method.

Due to the specific nature of the SRG, the total reference torque must be shared with adjacent phases, resulting in torque ripple during the switching period. Among various indirect torque control methods, TSF is the most useful and simplest method for reducing torque ripple [41]. The TSFs are categorized into linear and nonlinear types, with the non-linear category further classified as cubic, sinusoidal, and exponential TSFs [42]. These nonlinear TSFs prove effective at low speeds, resulting in minimized torque ripple. Figure 5a,b depict distinct curves for linear and sinusoidal TSFs, respectively. Our study primarily concentrates on sinusoidal TSFs.

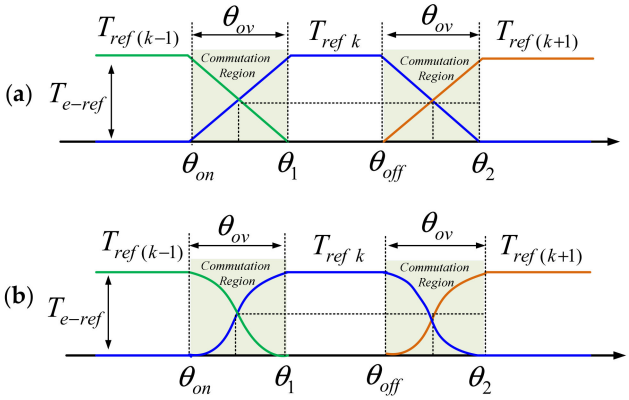

Figure 5. (**a**) Linear and (**b**) sinusoidal TSF functions.

To produce undulation-free torque, the reference torque is distributed to each phase using various distribution functions. The reference torque values for each phase are defined as follows [43,44]:

$$T_{ref-k} = \begin{cases} 0 & si\ 0 \le \theta \le \theta_{on} \\ T_{e-ref}\ f_{rise}(\theta) & si\ \theta_{on} \le \theta \le \theta_1 \\ T_{e-ref} & si\ \theta_1 \le \theta \le \theta_{off} \\ T_{e-ref}\ f_{fall}(\theta) & si\ \theta_{off} \le \theta \le \theta_2 \\ 0 & si\ \theta_2 \le \theta \le \theta_P \end{cases} \quad (14)$$

with

$$\theta_1 = \theta_{on} + \theta_{ov} \tag{15}$$

$$\theta_2 = \theta_{off} + \theta_{ov} \tag{16}$$

where $T_{e\text{-}ref}$, f_{rise}, and f_{fall} represent the reference torque, rising, and decreasing functions for consecutively triggered phases. θ_{on} and θ_{off}, and θ_{ov} represent the turn on, turn off, and overlap-angles. θ_p is the pole pitch, which is defined as follows, where N_r is the number of rotor poles:

$$\theta_P = \frac{2\pi}{N_r} \tag{17}$$

The incoming phase f_{rise} is defined as the rising TSF, defined as follows [45],

$$f_{rise}(\theta) = \frac{1}{2} - \frac{1}{2}\cos\left(\frac{\pi}{\theta_{ov}}(\theta - \theta_{on})\right) \tag{18}$$

The outgoing phase f_{fall} is defined as the falling TSF, given as follows [45],

$$f_{fall}(\theta) = \frac{1}{2} + \frac{1}{2}\cos\left(\frac{\pi}{\theta_{ov}}(\theta - \theta_{off})\right) \tag{19}$$

4. Control Scheme

Figure 4 shows the proposed speed control diagram for an SRG 8/6. In order to control the current and speed, the four-phase currents, rotor position, and speed are measured. Two main control loops are provided for the SRG drives: current and speed control loops. Within the primary current control loop, the measured four-phase currents are systematically compared with the reference currents through the implementation of a hysteresis controller. The secondary loop, the proposed speed control, acts on the reference and measured speed as inputs, and the reference torque is obtained as an output signal. Using (Equation (8)), the reference torque can be converted into a reference current as a function of the rotor position.

4.1. PI Controller

Figure 6 illustrates the block diagram of the closed-loop speed controller. The speed loop employs a PI controller, with the proportional and integral coefficients denoted as k_p and k_i, respectively. The transfer function of the PI controller is given as follows:

$$H(\mathrm{s}) = k_p + \frac{k_i}{s} \tag{20}$$

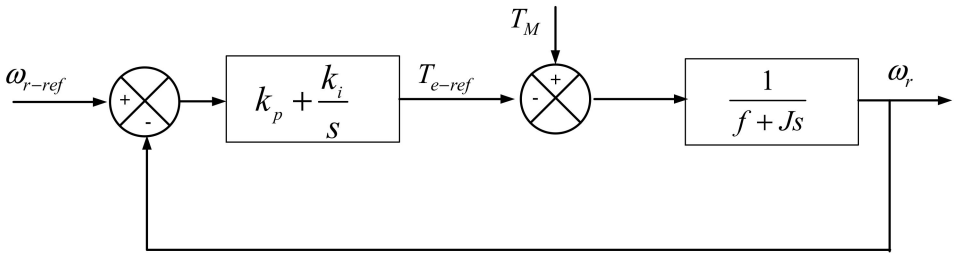

Figure 6. Diagram of a closed-loop PI speed controller.

Referring to Figure 6, the closed-loop transfer function can be obtained as follows:

$$G_{cl}(\mathrm{s}) = \frac{(k_p/k_i)s + 1}{(\mathrm{J}/k_i)s^2 + ((k_p + f)/k_i)s + 1} \tag{21}$$

The parameters of the speed controller are chosen to achieve the desired performance for the closed-loop system. After identifying the denominator in its canonical form, given in

(Equation (22)), the proportional and integral speed controller coefficients can be obtained by solving (Equation (23)).

$$G_{cl}(\mathrm{s}) = \frac{1}{(1/\omega_0^2)s^2 + (2\xi/\omega_0)s + 1} \tag{22}$$

$$\begin{array}{l} k_i = J\omega_0^2 \\ k_p = \frac{2\xi}{\omega_0}k_i - f \end{array} \tag{23}$$

4.2. Integral Sliding Mode Speed Controller

In traditional sliding mode control, the system's robustness to variations in parameters and external disturbances is attained exclusively during the sliding phase. However, the robustness is not assured during the reaching phase. In response to this challenge, integral sliding mode control eliminates the reaching phase, ensuring the enforcement of the sliding phase throughout the entire system response. To generate torque reference $T_{e\text{-}ref}$, we used the integral sliding mode speed controller. The mechanical equation is written as follows:

$$\dot{\omega_r} = \frac{1}{J}(\mathrm{T}_M - \mathrm{T}_e) - \frac{f}{J}\omega_r \tag{24}$$

Using desired state $\omega_r(\mathrm{t})$ and tracking error $e(\mathrm{t}) = \omega_{r-ref}(\mathrm{t}) - \omega_r(\mathrm{t})$, the sliding surface can be defined as follows:

$$S_\omega = e(\mathrm{t}) + \lambda_\omega \int_0^t e(\tau)d\tau, \;\; \lambda_\omega > 0 \tag{25}$$

where λ_ω is a positive constant. The control law can be represented by the following expression [46,47]:

$$\begin{array}{l} u(\mathrm{t}) = u_{eq}(\mathrm{t}) + u_d(\mathrm{t}) \\ u_{\min} < u < u_{\max} \Leftrightarrow \; u_{\min} - u_{eq} < u_d < u_{\max} - u_{eq} \\ or\ u_d = k\ sign(S_\omega) \\ \Leftrightarrow \forall S_\omega\ k \; < \; u_{\max} - u_{eq} \end{array} \tag{26}$$

where the equivalent control law U_{eq} is utilized to control the system behavior at the sliding surface, and the term U_d is a relay control function used to reject the disturbances and the parameter variations [47]. The discontinuous term U_d can be expressed as:

$$u_d(\mathrm{t}) = k\ sign(S_\omega) \tag{27}$$

where K is a positive constant. Due to its discontinuous nature, this term generates a chattering phenomenon that can be reduced utilizing a smooth control function. To find the equivalent command (U_{eq}), Equation (28) becomes, in our case:

$$S_\omega = \dot{S_\omega} = 0 \tag{28}$$

Thus, the following is obtained:

$$\dot{S_\omega} = \dot{e} + \lambda_\omega e = \dot{\omega}_{r-ref} - \left[\frac{1}{J}(\mathrm{T}_M - u) - \frac{f}{J}\omega_r\right] + \lambda_\omega e \tag{29}$$

Also, substitute Equation (25) into Equation (29) and consider, on the basis of Equation (28), that $U = U_{eq}$:

$$u_{eq} = J\left[\frac{1}{J}\mathrm{T}_M - \frac{f}{J}\omega - \dot{\omega}_{r-ref} - \lambda_\omega e\right] \tag{30}$$

Hence, the sliding mode speed controller is defined as follows:

$$T_{e-ref} = u_{eq} + u_d = J\left[\frac{1}{J}\mathrm{T}_M - \frac{f}{J}\omega - \dot{\omega}_{r-ref} - \lambda_\omega e\right] + k\ sign(S_\omega) \tag{31}$$

To verify the stability of the system, the Lyapunov function is proposed as [48]:

$$V = \frac{1}{2}S_\omega^2 \tag{32}$$

The stability is guaranteed if the following holds [49]:

$$\dot{V} = S_\omega \dot{S}_\omega < 0 \tag{33}$$

Consequently, the reachability condition of the sliding mode speed controller is verified as follows. The combination of Equations (29) and (33) gives:

$$\begin{aligned} \dot{V} &= S_\omega\left(\dot{\omega}_{r-ref} - \left[\tfrac{1}{J}\left(\mathrm{T}_M - T_{e-ref}\right) - \tfrac{f}{J}\omega_r\right] + \lambda_\omega e\right) \\ &= S_\omega\left(\underbrace{\left(\dot{\omega}_{r-ref} - \dot{\omega}_{r-ref} - \frac{f}{J}\omega_r + \frac{1}{J}\mathrm{T}_M - \lambda_\omega e - \frac{1}{J}\mathrm{T}_M + \frac{f}{J}\omega_r + \lambda_\omega e\right)}_{=0} - \tfrac{1}{J}k\ sign(S_\omega)\right) \\ &= -\tfrac{1}{J}S_\omega k\ sign(S_\omega) < 0 \end{aligned} \tag{34}$$

Figure 7 shows the block diagram of the ISMC. As shown in this figure, the real and reference speeds denote the inputs, and control signal $T_{e\text{-}ref}$ denotes the output.

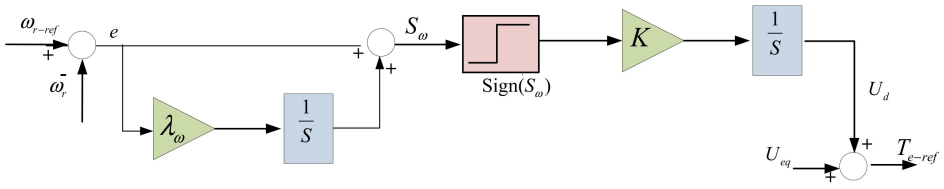

Figure 7. Block diagram of the ISMC for SRG drive.

The main drawback of ISMC is the difficulty of adjusting its gain, which is necessary to ensure a compromise between the controllers' disturbance rejection property and the chattering phenomenon. The ISMC law contains a discontinuity term. However, as a consequence of its discontinuous nature, it has certain limitations in electric drives and shows high-frequency oscillations in the form of chattering characteristics. This chattering produces various undesirable effects, such as current harmonics and torque pulsations in the drive train. To reduce the chattering, a super-twisting speed controller is proposed and developed in the next section.

4.3. Super-Twisting Rotor Speed Controller

A high-order sliding mode has been developed to overcome the limitations associated with the relative degree and to mitigate chattering in control systems [50]. Among various algorithms, STSMC stands out due to its ability to achieve finite-time convergence through continuous action without requiring information about derivatives of the sliding function [50]. This algorithm processes a relative degree equal to one, so it can directly replace standard sliding mode algorithms when the disturbance is smooth and with a gradient limited [51]. The super-twisting algorithm is used for systems with a relative degree equal to two. This algorithm does not require knowledge of the second derivative of the sliding surface, as other algorithms require. Thus, this algorithm guarantees that system trajectories are twisted around the origin in the phase diagram [52], as shown in Figure 8.

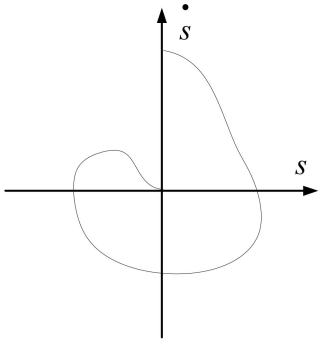

Figure 8. Convergence of STSMC.

Consider the following non-linear system:

$$\dot{S_\omega} = \phi(\mathrm{x},\mathrm{t}) + Y(\mathrm{x},\mathrm{t})u_{ST} \tag{35}$$

where S_ω is the sliding surface, U_{ST} is the control signal, and Φ and Y are uncertain functions with upper and lower bounds. To guarantee convergence of the sliding surface to zero in the presence of disturbances and uncertainties, the functions Φ and Y must verify the following conditions [53]:

$$\begin{cases} |\phi(\mathrm{x},\mathrm{t})| \leq \phi \\ Y_m < Y(\mathrm{x},\mathrm{t}) \leq Y_M \\ Y_m > 0 \end{cases} \tag{36}$$

According to Equations (24) and (25), the derivative of the surface is written as follows:

$$\begin{aligned} \dot{S_\omega} &= \dot{\omega}_{r-ref} - \left[\tfrac{1}{J}(\mathrm{T}_M - T_e) - \tfrac{f}{J}\omega_r\right] + \lambda_\omega e \\ &= \dot{\omega}_{r-ref} + \tfrac{1}{J}T_e + \tfrac{f}{J}\omega_{r-ref} - \tfrac{1}{J}\mathrm{T}_M + (\lambda_\omega - \tfrac{f}{J})e \end{aligned} \tag{37}$$

The STSMC control law is composed of two parts, U_1 and U_2, represented as follows [54]:

$$u_{ST} = u_1(t) + u_2(t) \tag{38}$$

with

$$\dot{u_1} = -\delta_\omega sign(S_\omega) \tag{39}$$

$$u_2 = -\mu_\omega |S_\omega|^\eta sign(S_\omega) + u_1 \tag{40}$$

where δ_ω and μ_ω are chosen as positive constants, and the parameter η presents the degree of nonlinearity. The sufficient conditions by Levant to offer a finite-time convergence are given as follows [55]:

$$\begin{cases} \delta_\omega \leq \frac{\phi}{Y_m} \\ \mu_\omega^2 = \frac{4\phi}{Y_m^2}\frac{Y_M(\delta_\omega+\phi)}{Y_m(\delta_\omega-\phi)} \\ 0 < \eta \leq 0.5 \end{cases} \tag{41}$$

where Y_m and Y_M are considered the bounds of the function Y. By identification, referring to Equation (35), the variables U_{ST}, Φ, and Y are:

$$\begin{cases} \phi = \left|\dot{\omega}_{r-ref} + \frac{f}{J}\omega_{r-ref} - \frac{1}{J}\mathrm{T}_M + (\lambda_\omega - \frac{f}{J})e\right| \\ Y = 1 \\ u_{ST} = \frac{1}{J}T_e \end{cases} \tag{42}$$

From Equation (42) and based the conditions of Equation (36), we have $0.5 < Y \leq 2$ and we can choose the following conditions:

$$\begin{cases} \delta_\omega = \frac{\phi}{0.5} = 2\,\phi \\ \mu_\omega^2 = \frac{4\phi}{0.5^2}\frac{2(2\,\phi+\phi)}{0.5(2\,\phi-\phi)} = 96\phi \\ \eta = 0.5 \end{cases} \tag{43}$$

Figure 9 depicts the block diagram of the STSMC. Within this illustration, the inputs are represented by the surface, while the output is denoted by the control signal $T_{e\text{-}ref}$.

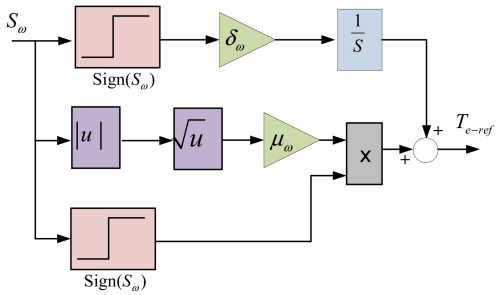

Figure 9. STSMC block diagram.

To provide a more detailed explanation of STSMC, the flow chart of the super-twisting algorithm is presented in Figure A1, located in Appendix A. The rapid responsiveness exhibited by STSMC renders it a compelling approach for managing nonlinear systems amidst uncertainty and disturbance. Nevertheless, real-world challenges, reliance on dynamic models, and adverse effects resulting from chattering may compromise control performance. To address these issues, intelligent methods, like fuzzy logic systems, can be employed to mitigate these limitations.

4.4. Fuzzy Super-Twisting Sliding Mode Command (FSTSMC)

This section presents the combination of STSMC with a Fuzzy Logic System (FLS) to reduce the undesirable effects of chatter in the presence of disturbances and model uncertainty. Therefore, the non-linear surface S_ω in Equation (25) and the derivative of surface is considered the input of the FLS of the control law. In this approach, the conventional sign function is replaced with the FLS. It is important to emphasize that chattering occurs when the system states are in proximity to $S_\omega = 0$. In the proposed solution, the FLS exhibits behavior similar to the sign function when the system states are distant from the sliding manifold [56]. The block diagram of the proposed FSTSMC is shown in Figure 10, which shows that the surface and its derivatives are the inputs, and control signal $u = T_{e\text{-}ref}$ is the output.

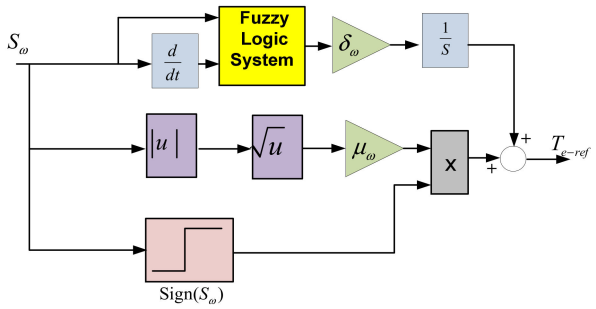

Figure 10. Block diagram of the proposed FSTSMC.

Conversely, when the states approach the sliding manifold closely, the FLS employs IF-THEN rules to mitigate the chattering phenomenon. Consequently, with this controller, the advantages of having a signum function in the SMC signal persist, as it continues to drive

the system states toward the sliding surface while effectively preventing chattering [57]. It is also possible to obtain the fuzzy approximate of the sign function directly from the system states. In this case, the MFs act on position error and its time derivative (see Figure 11). The rule base considered for this fuzzy system is summarized in Table 2, with N, Z, and P selected to be equal to −1, 0, and 1, respectively.

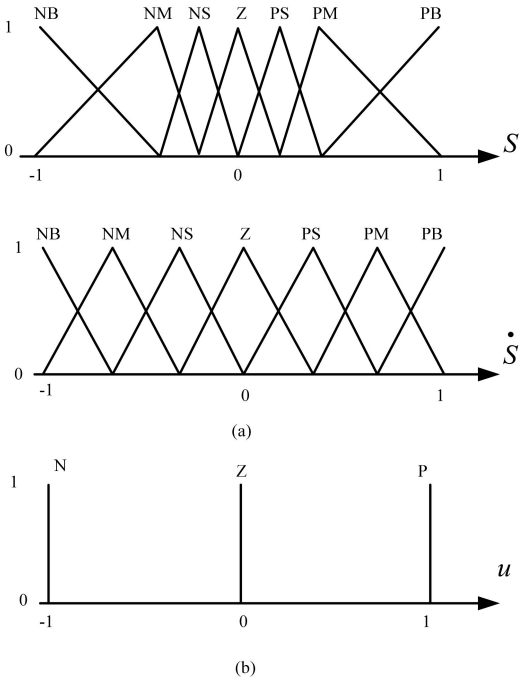

Figure 11. (**a**) Input membership function s and s dot; (**b**) output membership function.

Table 2. The fuzzy rule base for the more complex fuzzy system approximating the sign function.

dS/dt \ S	NB	NM	NS	Z	PS	PM	PB
NB	P	P	P	P	P	P	P
NM	N	P	P	P	P	P	P
NS	N	N	P	P	P	P	P
Z	N	N	N	Z	P	P	P
PS	N	N	N	N	N	P	P
PM	N	N	N	N	N	N	P
PB	N	N	N	N	N	N	N

5. Simulation Results

Current Controller

This section details the simulation of the current controller for the SRG drive using MATLAB®/SIMULINK® 2023. The hysteresis current controller band and sampling time are configured at 0.1 A and 50 µs, respectively. The regulation hysteresis of the currents of SRGs plays a crucial role in understanding and optimizing their performance. In simulation and experimental studies, a DC machine is often employed to emulate the mechanical power extracted from wind in wind turbines. To mimic the load, a variable resistance is used, and a shunt capacitor is employed to smooth the DC bus voltage. This setup allows for a comprehensive investigation into the dynamic behavior of the system under various conditions, shedding light on the intricate interactions between current regulation and the associated system parameters. Under controlled conditions, simulations were conducted to evaluate the impact of current variation on DC bus voltage.

The mechanical speed remained steadfast at 600 rpm, while the load resistance was initially fixed at a constant value of R_L = 400 Ω. The variation in the reference current significantly influences the behavior of the DC bus load, as illustrated in Figure 12. As the reference current undergoes changes, it directly impacts the overall system dynamics. The insight gained into the relationship between the reference current and the DC bus contributes to the development of strategies aimed at achieving the efficient and stable operation of SRGs. These strategies, informed by the observed effects on the DC bus, can be instrumental in enhancing the overall performance and reliability of SRG systems in various practical scenarios.

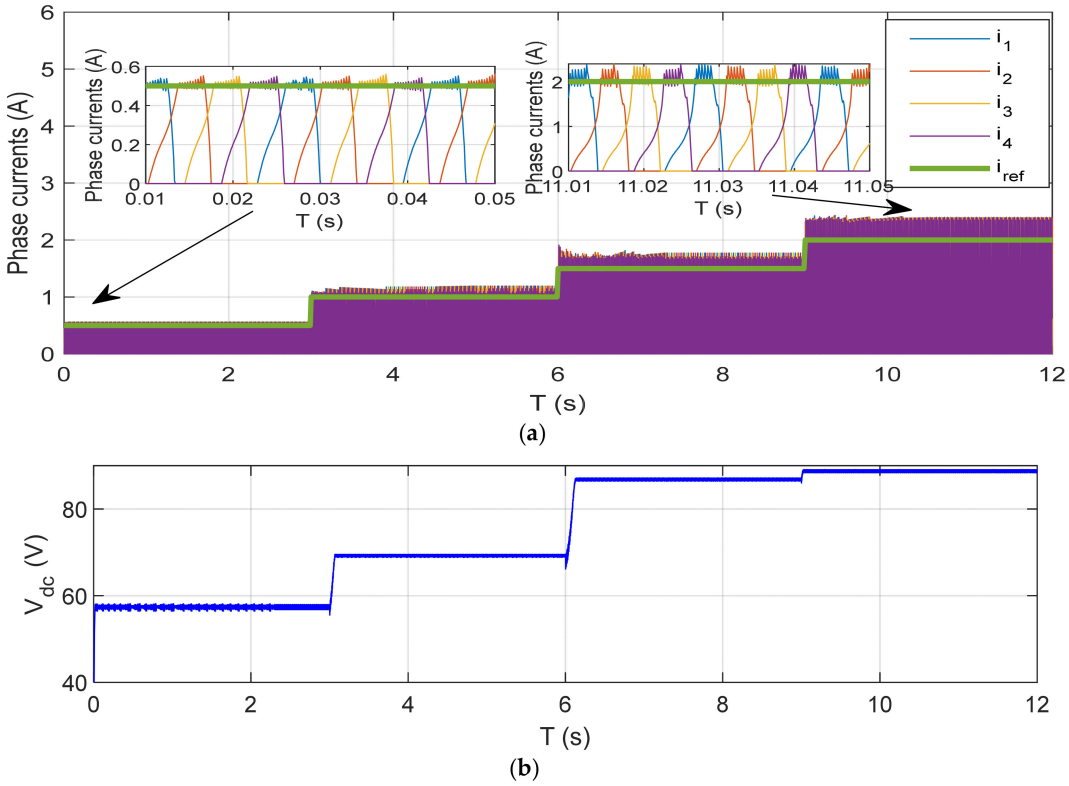

Figure 12. Effect of variation in reference current on DC bus: (**a**) phase currents of SRG; (**b**) DC bus voltage.

In addition to the reference current, the variation in the R_L (resistance of load) has a notable impact on the DC bus voltage. To evaluate the influence of load variation on DC bus voltage, simulations were conducted under controlled conditions. The mechanical speed was maintained at a constant 600 rpm, and the reference current was set to a fixed value of I_{ref} = 1 A. Notably, at t = 5 s, a significant change in the load occurred as it transitioned from 400 Ω to 333 Ω. Changes in the load parameters directly affected the voltage dynamics, influencing the stability and reliability of the system, as represented in Figure 13. Investigating this effect is fundamental in designing reluctance machines capable of adapting to diverse operating conditions.

To thoroughly assess the influence of speed variation on DC bus voltage, simulations were meticulously executed under controlled conditions. The load resistance remained constant at a value of R_L = 400 Ω, and the reference current was set to a fixed value of I_{ref} = 1 A. Initially, the wind turbine speed was established at w = 500 rpm. At t = 3 s, a deliberate change was introduced, increasing the speed from 500 rpm to 600 rpm. Subsequently, at t = 9 s, the wind turbine attained a final speed of 700 rpm. This carefully designed simulation provided a comprehensive understanding of the dynamic response of the system to varying wind turbine speeds.

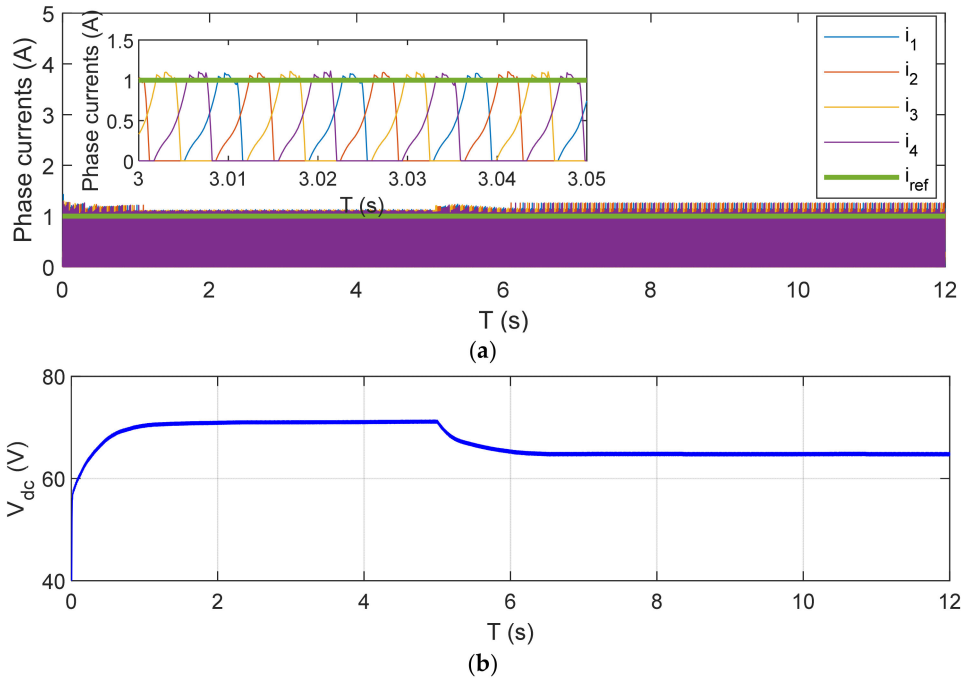

Figure 13. Effect of load variation on DC bus voltage: (**a**) phase currents of SRG; (**b**) DC bus voltage.

The fluctuation in wind turbine speed emerged as a pivotal factor significantly influencing the DC bus voltage. Variations in the speed of the wind turbine introduce dynamic changes to the mechanical power supplied to the DC machine, resulting in observable fluctuations in the DC bus voltage, as illustrated in Figure 14. This dynamic relationship between wind turbine speed and DC bus voltage is a key aspect of the system's behavior, which warrants careful analysis and consideration in the design and optimization of wind energy applications.

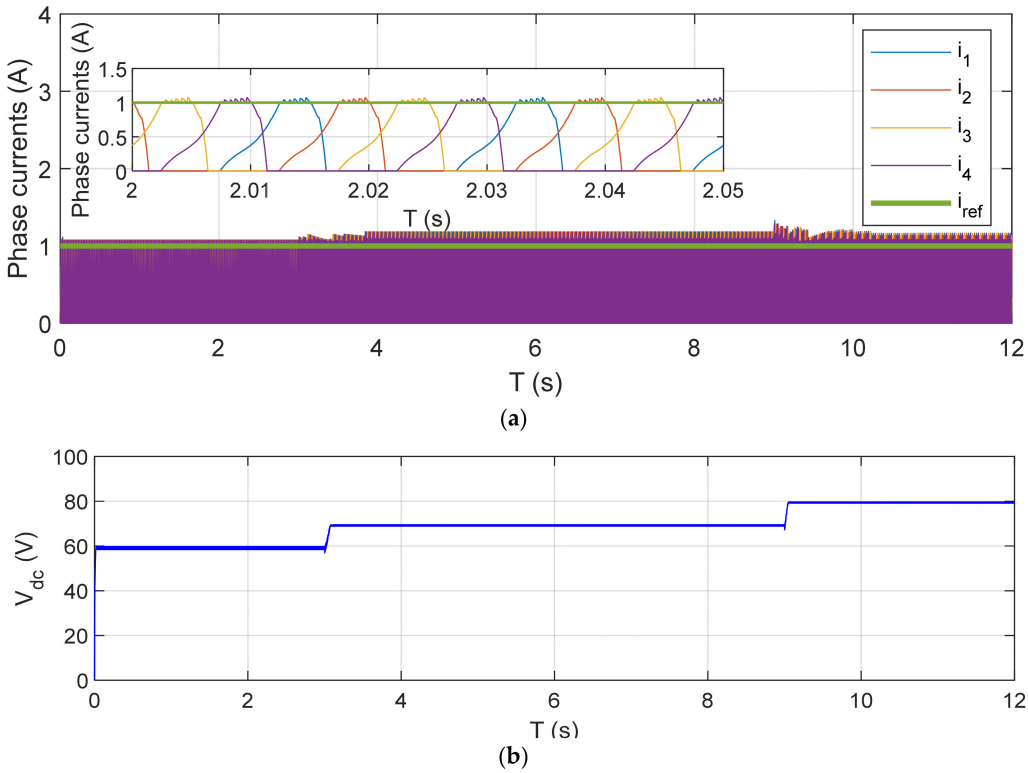

Figure 14. Effect of speed variation on DC bus voltage: (**a**) phase currents of SRG; (**b**) DC bus voltage.

The preceding section detailed and confirmed the current regulation, highlighting the multifaceted influence of various parameters on both current regulation and the DC bus. Building upon these findings, the subsequent section aims to further our understanding by exercising control over the turbine speed, maintaining it at a fixed value. From this set speed, we extracted the corresponding torque and reference current values. This deliberate approach allows us to explore the impact of controlling the turbine speed on the performance of the system. Specifically, our focus is directed toward the effect on the torque of the SRG. The overarching objective was to minimize torque ripple using various techniques. By investigating the interplay among turbine speed, torque, and reference current, we aim to develop strategies that effectively mitigate torque fluctuations, contributing to the overall optimization of SRG performance in our study.

Speed Controller

The simulation results of speed regulation, employing the indirect control method based on IITC with the FSF, are presented in this section. The validation of the simulation outcomes was conducted at a speed of 400 using the PI, ISMC, STSMC, and FSTSMC methods. The control parameters for each method are meticulously detailed in Table 3. This comprehensive evaluation allows us to assess the efficacy and performance of the indirect torque control strategy in regulating the speed of the system.

Table 3. Parameters of the control schemes.

Control Scheme	Parameters
PI	$k_p = 6.85$, $k_i = 0.02$
ISMC	K = 10, $\lambda_\omega = -0.001$
STSMC	δ_ω and μ_ω

High-performance applications, such as WECS, demand that the proposed design exhibits robustness in the face of parameter variations and external disturbances, with mechanical torque being a common source of disruption in the case of an SRG. To assess the robustness of the proposed FSTSMC, simulation tests are imperative, as the behavior of the SRG inherently suffers from ripples that can impact its speed and position feedback. Additionally, current feedback is prone to noise, which may indirectly contribute to an increase in speed ripples. Studying the performance of the FSTSMC under these conditions is crucial for ensuring the reliability and stability of SRGs in high-performance applications, particularly in scenarios where disturbances, variations, and inherent ripples can significantly affect the overall system behavior. Figures 15 and 16 illustrate the simulation results of speed control for the SRG using the PI, ISMC, STSMC, and FSTSMC methods at 400 rpm.

In Figure 15a,b the waveforms of the speed controller based on the PI controller and the ISMC method during the operation of the prime mover at 400 rpm are presented. These waveforms provide insights into the speed, total torque, currents, and current of one phase. Figure 16b highlights the superior performance of the FSTSMC, especially when the mechanical torque varies from 2 to 2.5 N-m at t = 4.0 s. Both controllers, STSMC and FSTSMC, were exposed to this torque change. The figure indicates that despite the sudden change in mechanical torque, the FSTSMC effectively maintained the desired speed without a significant drop in the prime mover speed and ensured a minimum reference pic current. In contrast, the STSMC struggled to achieve this level of performance and exhibited more pronounced speed oscillations during the period while attempting to compensate for the disturbance caused by the abrupt change in the speed of the prime mover.

In Figure 17, a comparison of the controllers is shown at 700 rpm. It can be seen that the higher-order sliding mode controller with the fuzzy logic system (FSTSMC) was more robust than STSMC.

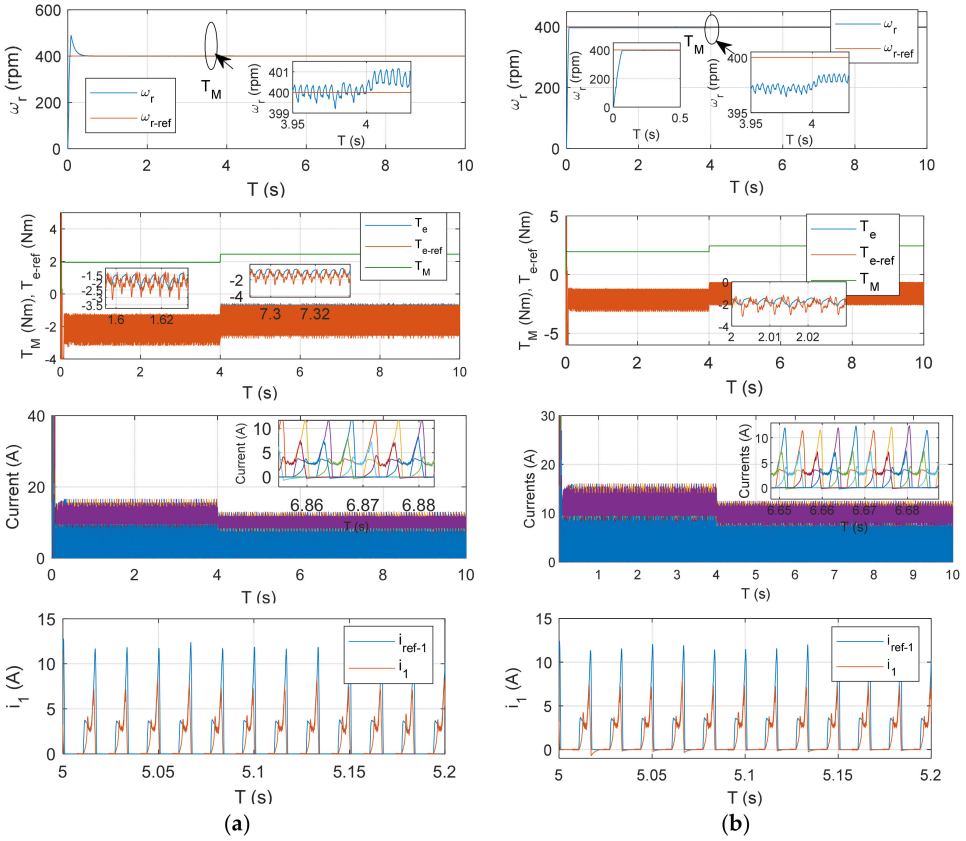

Figure 15. Simulation results at 400 rpm of speed, torque, and currents: (**a**) PI; (**b**) ISMC.

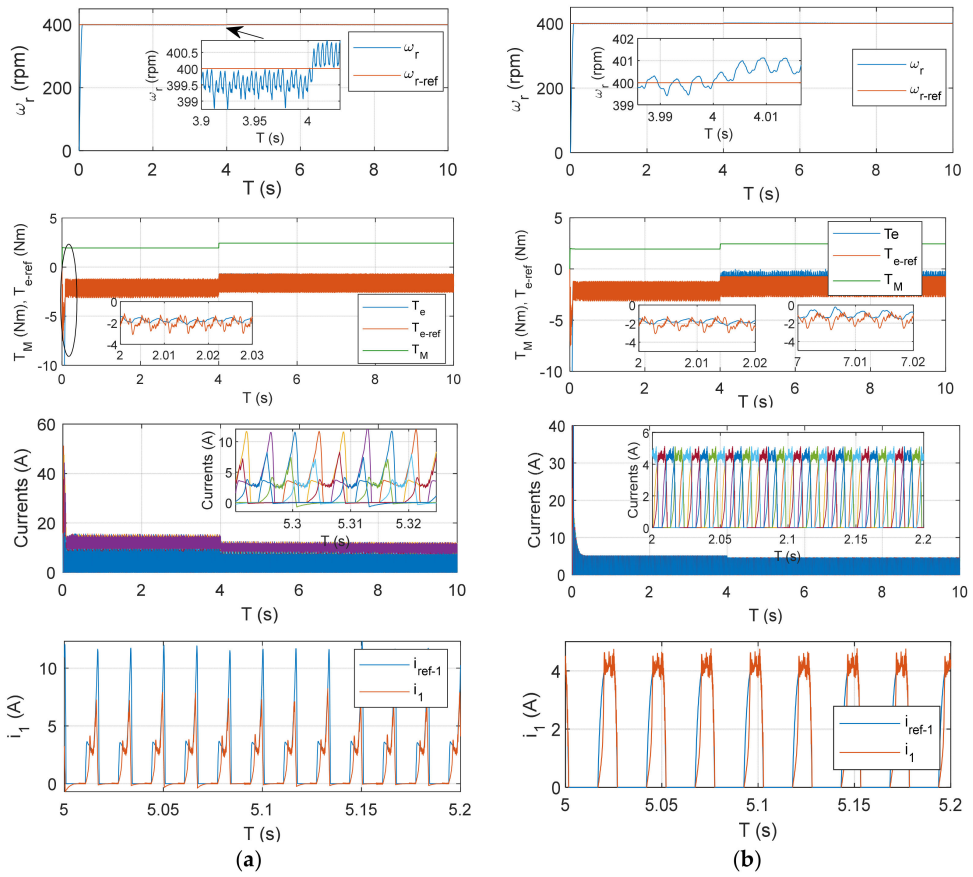

Figure 16. Simulation results at 400 rpm of speed, torque, and currents: (**a**) STSMC; (**b**) FSTSMC.

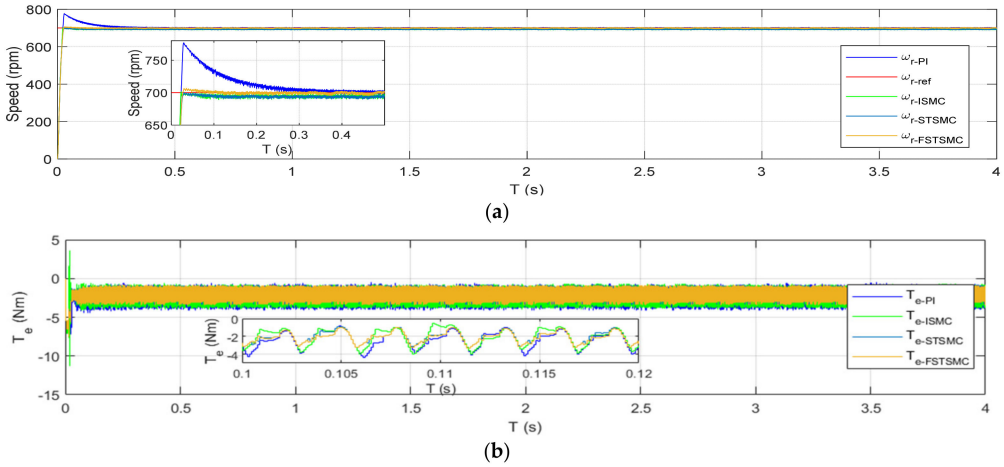

Figure 17. Simulation results at 700: (**a**) speed; (**b**) torque.

According to the simulation results, the proposed method successfully tracked the currents with a small tracking error and acceptable peak currents; hence, the torque error and torque ripple were minimized. It should be noted that eliminating the torque ripple improved the accuracy of the average torque and made it close to the reference value. The higher the ripple during the commutation, the larger the deviation of the average torque value from the reference value. While operating at high speeds, the current tracking error increased. Table 4 provides a comprehensive comparison of the four controllers, allowing for a quick assessment of their performance across key metrics. The results reaffirm the robustness of Fuzzy STSMC and its ability to outperform other controllers in terms of tracking accuracy, current peaks, torque ripple, and average torque deviation.

Table 4. Performances and robustness evaluation of different controllers.

Controller	Tracking Error	Peak Current	Torque Ripple	Average Torque Deviation
PI	Low	High	High	High
ISMC	Moderate	High	Moderate	Moderate
STSMC	High	High	Moderate	Moderate
FSTSMC (Proposed)	High	Low	Low	Low

6. Experimental Validation

Figure 18 illustrates the schematic of the testbed, comprising an inductance machine emulating the primary energy source and the current controller. The SRG features an 8/6 four-phase topology. An AHBC was employed to regulate the SRG's operation. This converter was activated by an external excitation source during magnetization mode and transferred power to the load (an equivalent resistance) through the DC bus during the generation mode with 58 V. The control segment encompassed a host PC for programming, supervision (MATLAB®/SIMULINK®, Control-Desk), and data acquisition. The digital controller consisted of a digital signal processor (TMS320F28379D, Texas Instruments, Dallas, TX, USA), responsible for current control.

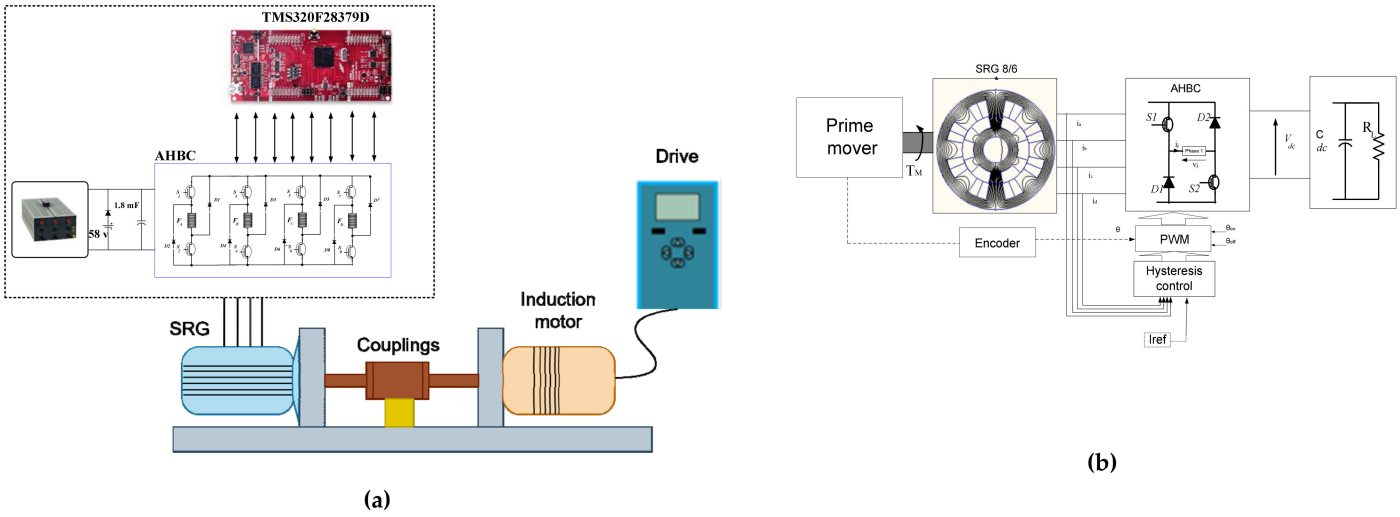

Figure 18. Experimental SRG drive. (**a**) Block diagram of testbench; (**b**) block diagram of current control.

In the pursuit of experimental validation, the focus was primarily directed toward the first segment of the current control methodology. The intention was to rigorously validate this specific aspect through practical experimentation.

The characteristics of the SRG used in this paper are detailed in Table 5.

Table 5. Database of 8/6 SRG.

Characteristics	Values
Output power	250 W
Maximum current	3 A
Inductance (aligned position)	0.14 H
Inductance (unaligned position)	0.021 H
Moment of inertia	0.006 kg m^2
Resistance of phase winding	5 Ω

The DC voltage generated is influenced by various factors, including the phase current reference (I_{ref}), speed (ω_r), and load (R_L). Preliminary experimental tests have been conducted to comprehensively analyze how these parameters impact the DC bus voltage. Figure 19 highlights the notable influence of the phase current reference on the DC bus voltage of the SRG. These findings are in concurrence with the simulation results obtained in Figure 12, with only the presence of minor ripples in the DC bus voltage. Additionally, Figure 20 illustrates the dynamic response of the DC voltage to load step changes, indicating an increase in the DC voltage when the load current decreases, corresponding to an increase in resistance. These results align consistently with the simulation outcomes depicted in Figure 13, where only minor ripples are observed in the DC bus voltage. The convergence between experimental and simulation results underscores the reliability and accuracy of the proposed hysteresis control. Furthermore, in Figure 21, the response of the DC bus to a speed step change is depicted, illustrating the rise in the DC voltage corresponding to the change in speed. These observations align consistently with the simulation results presented in Figure 14. These preliminary experimental results emphasize the significant impact of three key parameters of the SRG operation. It is further demonstrated that electrical power generation and its efficiency are intricately dependent on these independent parameters.

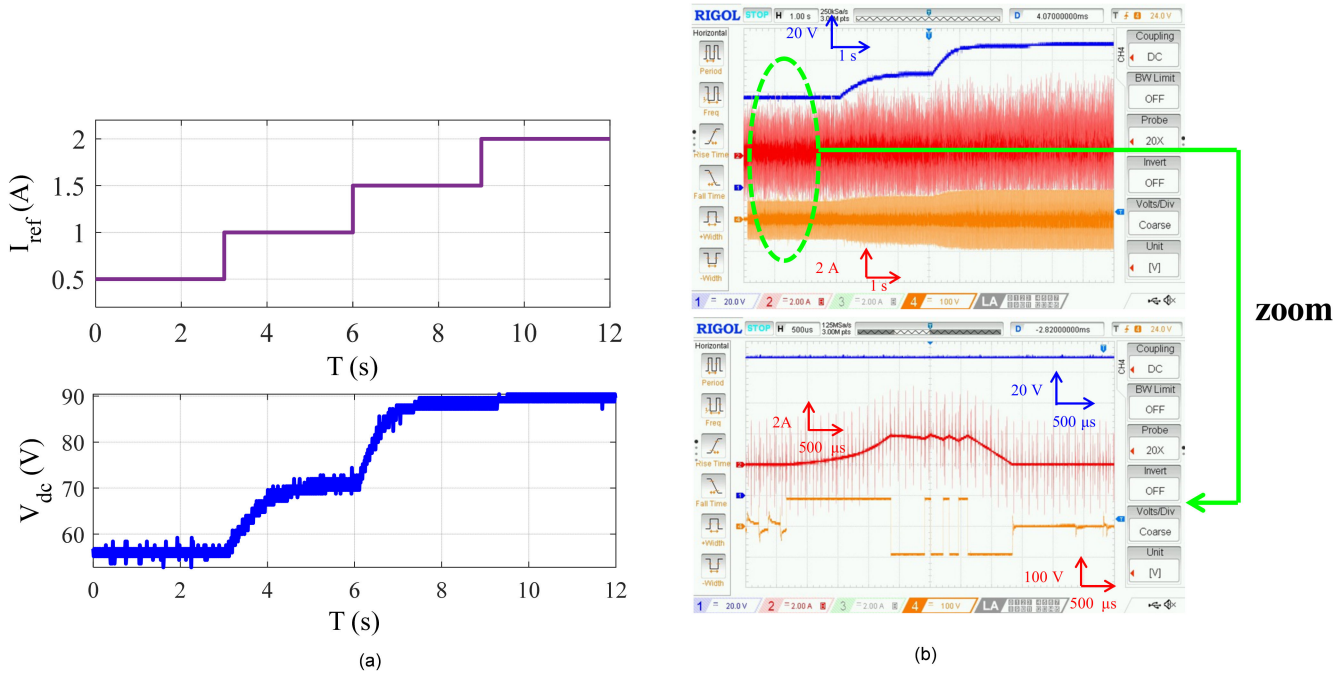

Figure 19. Experimental results of the effect of current variation. All other parameters were set to: ω_r = 600 rpm and R_L = 400 Ω. (**a**) DC bus voltage; (**b**) current and voltage of phase 1.

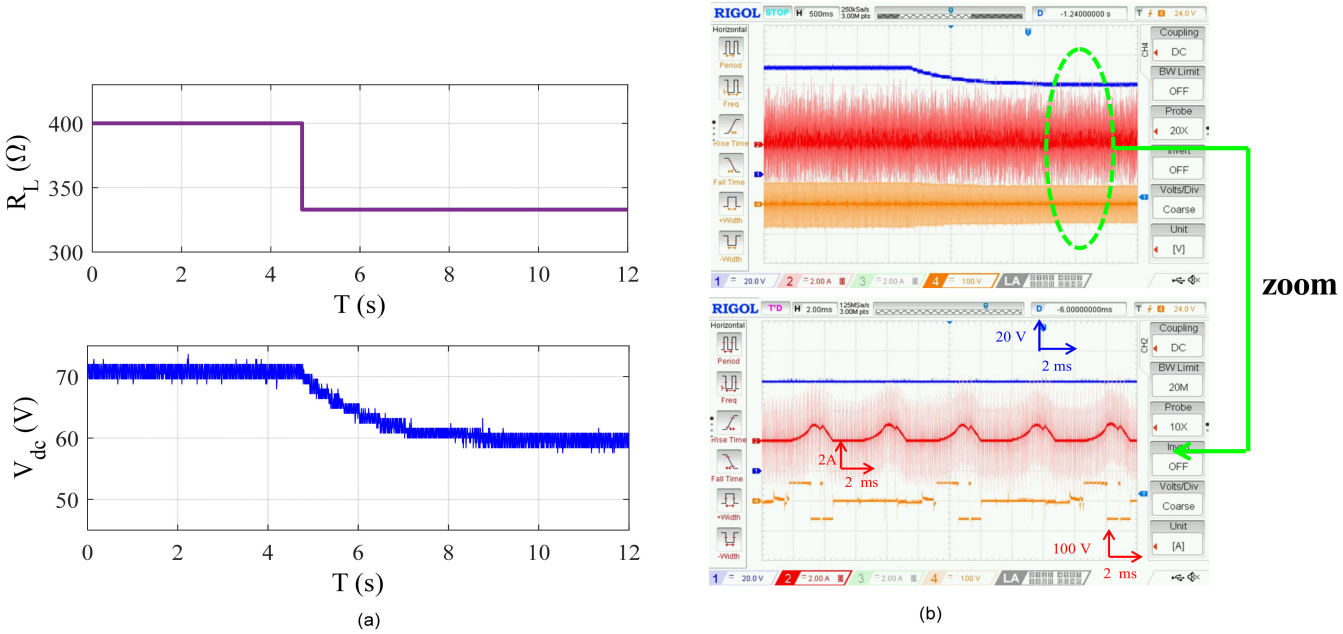

Figure 20. Experimental results of load variation effect. All other parameters were set to: ω_r = 600 rpm and I_{ref} = 1 A. (**a**) DC bus voltage; (**b**) current and voltage of phase 1.

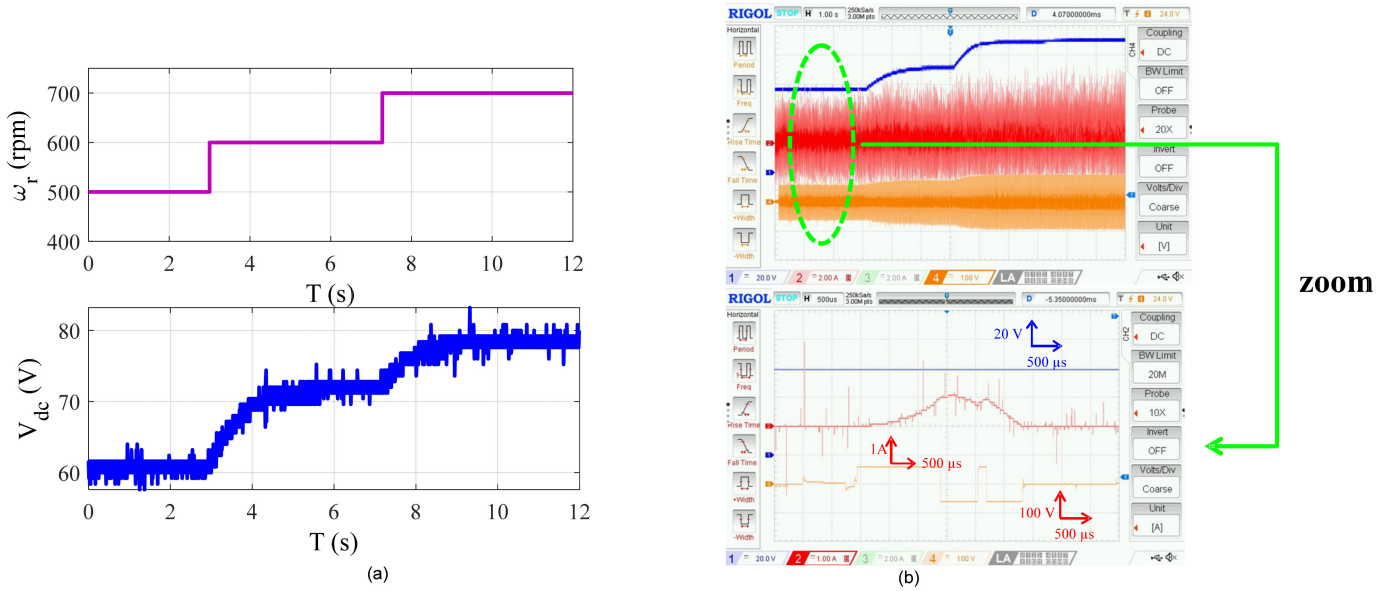

Figure 21. Experimental results of the effect of speed variation on the DC bus voltage. All other parameters were set to: R_L = 400 Ω and I_{ref} = 1 A.

7. Conclusions

This paper introduces a novel control strategy for switched reluctance generators applied to WECS for low-voltage DC microgrids. A torque sharing method based on indirect instantaneous torque control is presented. A performance comparison of the speed control of SRGs with a FSTSMC, ISMC, STSMC, and conventional PI controller was carried out in this study. Despite their simplicity of design and ease of implementation, PI controllers exhibited moderate performance under undisturbed conditions. However, their limitations became apparent under disturbed conditions, such as sudden changes in reference speed, leading to substantial overshoot and an extended settling time. In the time domain, the suggested FSTSMC showcased a faster rise time under speed variation when compared to both the proportional–integral control and conventional sliding mode control methods. Moreover, the proposed fuzzy STSMC performed well in terms of the speed and torque ripple. The proposed control strategy combines the advantages of fast and finite-time convergence of tracking error under load disturbance while mitigating chattering effects. The simulation results validate the effectiveness of the proposed method, showcasing its potential for enhancing the speed control performance of SRGs in WECS. The effectiveness of the current control strategy has been assessed through both numerical simulations and experimental tests conducted on an SRG-based drive supplying a variable DC load. This dual evaluation approach, encompassing theoretical simulations and practical experiments, provides a comprehensive understanding of the control strategy's performance under varying conditions. In the future, our efforts will focus on testing the speed control loop in a laboratory. Thanks to these advances, we expect to improve the reliability and efficiency of the control strategy of SRG for WECS applications.

Author Contributions: Conceptualization, Z.T., I.M., R.E.A. and A.K.; methodology, Z.T., I.M., R.E.A. and A.K.; software, Z.T. and I.M.; validation, Z.T., I.M., R.E.A. and A.K.; formal analysis, Z.T., I.M., R.E.A. and A.K.; investigation, Z.T., I.M., R.E.A. and A.K.; resources, R.E.A. and A.K.; data curation, Z.T. and A.K.; writing—original draft preparation, Z.T. and R.E.A.; writing—review and editing, Z.T., I.M., R.E.A. and A.K.; supervision, R.E.A. and A.K.; project administration, Z.T., I.M., R.E.A. and A.K.; funding acquisition, R.E.A. and A.K. All authors have read and agreed to the published version of the manuscript.

Funding: This work is financed by National Funds through the Portuguese funding agency, FCT—Fundação para a Ciência e a Tecnologia, within project LA/P/0063/2020. DOI 10.54499/LA/P/0063/2020 | https://doi.org/10.54499/LA/P/0063/2020.

Data Availability Statement: The raw data supporting the conclusions of this article will be made available by the authors on request.

Conflicts of Interest: The authors declare no conflicts of interest.

Appendix A

Figure A1 depicts a flow chart for the Super-Twisting Rotor Speed Controller.

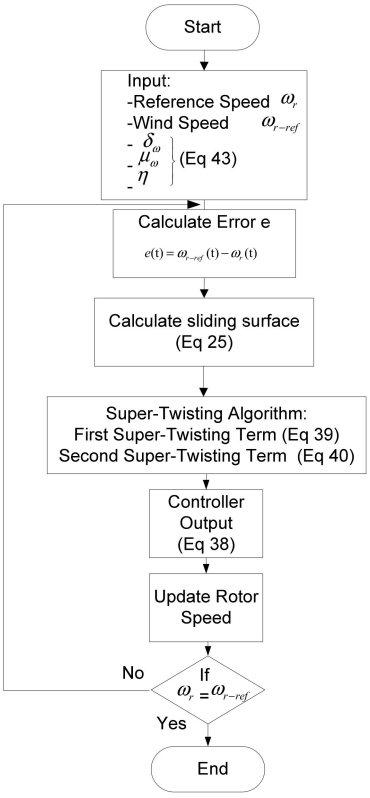

Figure A1. Flowchart of STSMC.

This graphical representation provides a concise and intuitive overview of the control algorithm's sequential steps and interactions, complementing the detailed formulations presented in the manuscript.

References

1. Ayop, R.; Tan, C.W. Design of boost converter based on maximum power point resistance for photovoltaic applications. *Solar Energy* **2018**, *160*, 322–335. [CrossRef]
2. Cheng, M.; Zhu, Y. The state of the art of wind energy conversion systems and technologies: A review. *Energy Convers. Manag.* **2014**, *88*, 332–347. [CrossRef]
3. Rahmanian, E.; Akbari, H.; Sheisi, G. Maximum Power Point Tracking in Grid Connected Wind Plant by Using Intelligent Controller and Switched Reluctance Generator. *IEEE Trans. Sustain. Energy* **2017**, *8*, 1313–1320. [CrossRef]
4. Namazi, M.M.; Koofigar, H.R.; Ahn, J.W. Active Stabilization of Self-Excited Switched Reluctance Generator Supplying Constant Power Load in DC-microgrids. *IEEE J. Emerg. Sel. Top. Power Electron.* **2020**, *9*, 2735–2744. [CrossRef]
5. Yi, F.; Wen, C. Control and Seamless Transition of Bi-Directional Battery-Driven Switched Reluctance Motor/Generator Drive Based on Integrated Multiport Power Converter for Electric Vehicle Applications. *IEEE Trans. Power. Electron.* **2015**, *31*, 7099–7111. [CrossRef]
6. Krishna, B.; Sandeep, V. *An Analytical Study on Electric Generators and Load Control Schemes for Small Hydro Isolated Systems*; Springer: Cham, Switzerland, 2021; pp. 103–119.

7. de Paula, M.V.; Barros, T.A.d.S. A sliding mode ditc cruise control for srm with steepest descent minimum torque ripple point tracking. *IEEE Trans. Ind. Electron.* **2022**, *69*, 151–159. [CrossRef]
8. Zhao, S.; Chen, H.; Nie, R.; Liu, J. Multi-objective optimal design of double-sided switched reluctance linear generator for wave power generation. *COMPEL Int. J. Comput. Math. Electr. Electron. Eng.* **2019**, *38*, 1948–1963. [CrossRef]
9. Roshandel, E.; Namazi, M.M.; Rashidi, A.; Saghaian-Nejad, S.M.; Ahn, J.W. SSC Strategy for SRG to Achieve Maximum Power with Minimum Current Ripple in Battery Charging. *IET Electr. Power Appl.* **2017**, *11*, 1205–1213. [CrossRef]
10. Zhan, Y.; Chen, H.; Hua, M.; Liu, J.; He, H.; Wheeler, P.; Fernao Pires, V. Multi-objective optimization design of novel tubular switched reluctance motor. *COMPEL Int. J. Comput. Math. Electr.* **2023**, *42*, 1434–1455. [CrossRef]
11. Touati, Z.; Araújo, R.E.; Mahmoud, I.; Khedher, A. Analysis of skewing effects on radial force for different topologies of switched reluctance machines: 6/4 SRM, 8/6 SRM, and 12/8 SRM. *Univ. Porto J. Eng.* **2023**, *9*, 55–71. [CrossRef]
12. Touati, Z.; Pereira, M.; Araújo, R.E.; Khedher, A. Integration of Switched Reluctance Generator in a Wind Energy Conversion System: An Overview of the State of the Art and Challenges. *Energies* **2022**, *15*, 4743. [CrossRef]
13. Scalcon, F.P.; Fang, G.; Volpato Filho, C.J.; Gründling, H.A.; Vieira, R.P.; Nahid-Mobarakeh, B. A review on switched reluctance generators in wind power applications: Fundamentals, control and future trends. *IEEE Access* **2022**, *10*, 69412–69427. [CrossRef]
14. Dos Santos Neto, P.J.; dos Santos Barros, T.A.; de Paula, M.V.; de Souza, R.R.; Silveira, J.P.C.; Ruppert Filho, E. DC-microgrid with Wind Energy Conversion System Based on Switched Reluctance Generator Operating in Grid Connected Mode. In Proceedings of the 13th IEEE International Conference on Industry Applications (INDUSCON), São Paolo, Brazil, 11–14 November 2018.
15. Dos Santos Neto, P.J.; dos Santos Barros, T.A.; Catata, E.H.; Ruppert Filho, E. Grid-Connected SRG Interfaced with Bidirectional DC-DC Converter in WECS. *IEEE Trans. Energy Convers.* **2021**, *36*, 3261–3270. [CrossRef]
16. Touati, Z.; Pereira, M.; Araújo, R.E.; and Khedher, A. Comparative Study of Discrete PI and PR Controller Implemented in SRG for Wind Energy Application: Theory and Experimentation. *Electronics* **2022**, *11*, 1285. [CrossRef]
17. Osorio, C.R.; Vieira, R.P.; Grundling, H.A. Sliding Mode Technique Applied to Output Voltage Control of the Switched Reluctance Generator. In Proceedings of the 42nd Annual Conference of the IEEE Industrial Electronics Society, Florence, Italy, 24–27 October 2016.
18. Liu, Y.Z.; Zhou, Z.; Song, J.L.; Fan, B.J.; Wang, C. Based on Sliding Mode Variable Structure of Studying Control for Status Switching of Switched Reluctance Starter/Generator. In Proceedings of the 2015 Chinese Automation Congress (CAC), Wuhan, China, 27–29 November 2015; IEEE: New York, NY, USA, 2015; pp. 934–939.
19. Genc, U.; Tekgun, B. Instantaneous torque error compensation based online torque sharing function for Switched reluctance Machines. *Alex. Eng. J.* **2023**, *75*, 261–270. [CrossRef]
20. Gan, C.; Chen, Y.; Sun, Q.; Si, J.; Wu, J.; Hu, Y. position sensorless torque control strategy for switched reluctance machines with fewer current sensors. *IEEE/ASME Trans. Mechatron.* **2020**, *26*, 1118–1128. [CrossRef]
21. Valencia, D.F.; Tarvirdilu-Asl, R.; Garcia, C.; Rodriguez, J.; Emadi, A. A review of predictive control techniques for switched reluctance machine drives. Part II: Torque control, assessment and challenges. *IEEE Trans. Energy Convers.* **2020**, *36*, 1323–1335. [CrossRef]
22. Yan, N.; Cao, X.; Deng, Z. Direct torque control for switched reluctance motor to obtain high torque–ampere ratio. *IEEE Trans. Ind. Electron.* **2018**, *66*, 5144–5152. [CrossRef]
23. Zine, M.; Chemsa, A.; Labiod, C.; Ikhlef, M.; Srairi, K.; Benbouzid, M. Coupled Indirect Torque Control and Maximum Power Point Tracking Technique for Optimal Performance of 12/8 Switched Reluctance Generator-Based Wind Turbines. *Machines* **2022**, *10*, 1046. [CrossRef]
24. Zine, M.; Chemsa, A.; Labiod, C.; Ikhlef, M.; Srairi, K.; Benbouzid, M. Improving Efficiency and Power Output of Switched Reluctance Generators through Optimum Operating Parameters. *Machines* **2023**, *11*, 816. [CrossRef]
25. Hancco Catata, E.O.; de Paula, M.V.; dos Santos Neto, P.J.; Ruppert Filho, E.; Luque Carcasi, D.B.; dos Santos Barros, T.A. Direct Average Torque Control of Switched Reluctance Generator. *IET Power Electron.* **2023**, *12*, 2011–2021. [CrossRef]
26. Shin, H.U.; Park, K.; Lee, K.B. A Non-Unity Torque Sharing Function for Torque Ripple Minimization of Switched Reluctance Generators in Wind Power Systems. *Energies* **2015**, *8*, 11685–11701. [CrossRef]
27. Liu, Y.C.; Laghrouche, S.; Depernet, D.; N'Diaye, A.; Djerdir, A.; Cirrincione, M. Disturbance-observer-based speed control for SPMSM drives using modified super-twisting algorithm and extended state observer. *Asian J. Control* **2023**. [CrossRef]
28. Civelek, Z. Optimization of fuzzy logic (Takagi-Sugeno) blade pitch angle controller in wind turbines by genetic algorithm. *Eng. Sci. Technol. Int. J.* **2020**, *23*, 1–9. [CrossRef]
29. Rodríguez Pérez, Á.M.; Rodríguez, C.A.; Olmo Rodríguez, L.; Caparros Mancera, J.J. Revitalizing the Canal de Castilla: A Community Approach to Sustainable Hydropower Assessed through Fuzzy Logic. *Appl. Sci.* **2024**, *14*, 1828. [CrossRef]
30. Prasad, K.A.; Unnikrishnan, A.; Nair, U. Fuzzy sliding mode control of a switched reluctance motor. *Procedia Technol.* **2016**, *25*, 735–742. [CrossRef]
31. Divandari, M.; Rezaie, B.; Noei, A.R. Speed control of switched reluctance motor via fuzzy fast terminal sliding-mode control. *Comput. Electr. Eng.* **2019**, *80*, 106472. [CrossRef]
32. Sehab, R.; Akrad, A.; Saadi, Y. Super-Twisting Sliding Mode Control to Improve Performances and Robustness of a Switched Reluctance Machine for an Electric Vehicle Drivetrain Application. *Energies* **2023**, *16*, 3212. [CrossRef]
33. Rafiq, M.; Rehman, S.U.; Rehman, F.U.; Butt, Q.R.; Awan, I. A second order sliding mode control design of a switched reluctance motor using super twisting algorithm. *Simul. Model. Pract. Theory* **2012**, *25*, 106–117. [CrossRef]

34. Bilgin, B.; Jiang, J.W.; Emadi, A. (Eds.) *Switched Reluctance Motor Drives: Fundamentals to Applications*; CRC Press: Boca Raton, FL, USA, 2019.
35. Costa, J.V.; Branco, P.J. Sensorless Switched Reluctance Machine and Speed Control: A Study to Remove the Position Encoder at High Speed of Operation. *Energies* **2022**, *15*, 1716. [CrossRef]
36. Singh, B.; Bhuvaneswari, G. Position Sensor-Less Synchronous Reluctance Generator Based Grid-Tied Wind Energy Conversion System with Adaptive Observer Control. *IEEE Trans. Sustain. Energy* **2019**, *11*, 693–702.
37. Xia, Y.; Ahmed, K.H.; Williams, B.W. Wind Turbine Power Coefficient Analysis of a New Maximum Power Point Tracking Technique. *IEEE Trans. Ind. Electron.* **2012**, *60*, 1122–1132. [CrossRef]
38. Bouchoucha, K.; Yahia, H.; Mansouri, M.N. Particle Swarm Optimization of Switched Reluctance Generator Based Distributed Wind Generation. *J. Multidiscip. Eng. Sci. Technol.* **2014**, *1*, 107–113.
39. Al Quraan, L.; Szamel, L. Torque ripple reduction of switched reluctance motor using direct instantaneous torque control and adaptive turn-on technique for electric vehicle applications. *IET Electr. Power Appl.* **2023**, *17*, 1502–1514. [CrossRef]
40. Sahoo, S.K.; Panda, S.K.; Xu, J.X. Indirect Torque Control of Switched Reluctance Motors Using Iterative Learning Control. *IEEE Trans. Power Electron.* **2005**, *20*, 200–208. [CrossRef]
41. Feng, L.; Sun, X.; Yang, Z.; Diao, K. Optimal Torque Sharing Function Control for Switched Reluctance Motors Based on Active Disturbance Rejection Controlle. *IEEE/ASME Trans. Mechatron.* **2023**, *28*, 2600–2608. [CrossRef]
42. Hu, H.; Cao, X.; Yan, N.; Deng, Z. A New Predictive Torque Control Based Torque Sharing Function for Switched Reluctance Motors. In Proceedings of the 2019 22nd International Conference on Electrical Machines and Systems (ICEMS), Harbin, China, 11–14 August 2019; pp. 1–5.
43. Al-Amyal, F.; Al Quraan, L.; Szamel, L. Torque Sharing Function Optimization for Extended Speed Range Control in Switched Reluctance Motor Drive. In Proceedings of the IEEE 3rd International Conference and Workshop in Óbuda on Electrical and Power Engineering (CANDO-EPE), Budapest, Hungary, 18–20 November 2020.
44. Ye, W.; Ma, Q.; Zhang, P.; Guo, Y. Torque Ripple Reduction in Switched Reluctance Motor Using a Novel Torque Sharing Function. In Proceedings of the 2016 IEEE International Conference on Aircraft Utility Systems (AUS), Beijing, China, 10–12 October 2016; pp. 177–182.
45. Pop, A.C.; Petrus, V.; Martis, C.S.; Iancu, V.; Gyselinck, J. Comparative Study of Different Torque Sharing Functions for Losses Minimization in Switched Reluctance Motors Used in Electric Vehicles Propulsion. In Proceedings of the 2012 13th International Conference on Optimization of Electrical and Electronic Equipment (OPTIM), Brasov, Romania, 24–26 May 2012; pp. 356–365.
46. Krim, S.; Gdaim, S.; Mimouni, M.F. Robust Direct Torque Control with Super-Twisting Sliding Mode Control for an Induction Motor Drive. *Complexity* **2019**, *2019*, 7274353. [CrossRef]
47. Sami, I.; Ullah, S.; Basit, A.; Ullah, N.; Ro, J.S. Integral Super Twisting Sliding Mode Based Sensorless Predictive Torque Control of Induction Motor. *IEEE Access* **2020**, *8*, 186740–186755. [CrossRef]
48. Dursun, E.H.; Durdu, A. Speed Control of a DC Motor with Variable Load Using Sliding Mode Control. *Int. J. Comput. Electr. Eng.* **2016**, *8*, 219. [CrossRef]
49. Benkhoris, M.F.; Gayed, A. Discrete Sliding Control Technique of DC Motor Drives. In Proceedings of the Sixth IEEE International Conference on Power Electronics and Variable Speed Drives, Nottingham, UK, 23–25 September 1996.
50. Levant, A. Robust Exact Differentiation via Sliding Mode Technique. *Automatica* **1998**, *34*, 379–384. [CrossRef]
51. Picó, J.; Picó-Marco, E.; Vignoni, A.; De Battista, H. Stability Preserving Maps for Finite-Time Convergence: Super-Twisting Sliding-Mode Algorithm. *Automatica* **2013**, *49*, 534–539. [CrossRef]
52. Horch, M.; Boumédiène, A.; Baghli, L. Backstepping Approach for Nonlinear Super Twisting Sliding Mode Control of an Induction Motor. In Proceedings of the 2015 3rd International Conference on Control, Engineering & Information Technology (CEIT), Tlemcen, Algeria, 25–27 May 2015; pp. 1–6.
53. Ouchen, S.; Benbouzid, M.; Blaabjerg, F.; Betka, A.; Steinhart, H. Direct Power Control of Shunt Active Power Filter Using Space Vector Modulation Based on Supertwisting Sliding Mode Control. *IEEE J. Emerg. Sel. Top. Power Electron.* **2020**, *9*, 3243–3253. [CrossRef]
54. Lascu, C.; Blaabjerg, F. Super-Twisting Sliding Mode Direct Torque Control of Induction Machine Drives. In Proceedings of the 2014 IEEE Energy Conversion Congress and Exposition (ECCE), Pittsburgh, PA, USA, 14–18 September 2014; pp. 5116–5122.
55. Levant, A. Higher-Order Sliding Modes, Differentiation and Output Feedback Control. *Int. J. Control* **1998**, *76*, 924–941. [CrossRef]
56. Benbouhenni, H. Fuzzy Second Order Sliding Mode Controller Based on Three-Level Fuzzy Space Vector Modulation of a DFIG for Wind Energy Conversion Systems. *Majlesi J. Mechatron. Syst.* **2018**, *7*, 17–26.
57. Palm, R. Sliding Mode Fuzzy Control. In Proceedings of the [1992 Proceedings] IEEE International Conference on Fuzzy Systems, San Diego, CA, USA, 8–12 March 1992; pp. 519–526.